Additive Manufacturing 34 (2020) 101386

Contents lists available at ScienceDirect

Additive Manufacturing

journal homepage: www.elsevier.com/locate/addma

In situ investigation into temperature evolution and heat generation during additive friction stir deposition: A comparative study of Cu and Al-Mg-Si

David Garcia[a], W. Douglas Hartley[a], Hunter A. Rauch[a], R. Joey Griffiths[a], Rongxuan Wang[b], Zhenyu J. Kong[b], Yunhui Zhu[c], Hang Z. Yu[a,*]

[a] Department of Materials Science and Engineering, Virginia Tech, 435 Turner St NW, Blacksburg, VA 24061, USA
[b] Department of Industrial and System Engineering, Virginia Tech, 1145 Perry St, Blacksburg, VA 24061, USA
[c] Department of Electrical and Computer Engineering, Virginia Tech, 1185 Perry Street, Blacksburg, VA 24061, USA

ARTICLE INFO

Keywords:
In situ monitoring
Temperature evolution
Heat generation
Materials flow
Solid-state additive manufacturing

ABSTRACT

Additive friction stir deposition is an emerging solid-state additive manufacturing technology that enables site-specific build-up of high-quality metals with fine, equiaxed microstructures and excellent mechanical properties. By incorporating proper machining, it has the potential to produce large-scale, complex 3D geometries. Still early in its development, a thorough understanding of the thermal process fundamentals, including temperature evolution and heat generation mechanisms, has not been established. Here, we aim to bridge this gap through *in situ*monitoring of the thermal field and material flow behavior using complementary infrared imaging, thermocouple measurement, and optical imaging. Two materials challenging to print via beam-based additive technologies, Cu and Al-Mg-Si, are investigated. During additive friction stir deposition of both materials, we find similar trends of thermal features (e.g., the trends of peak temperature T_{Peak}, exposure time, and cooling rate) with respect to the processing conditions (e.g., the tool rotation rate Ω and in-plane velocity V). However, there is a salient, quantitative difference between Cu and Al-Mg-Si; T_{Peak} exhibits a power law relationship with Ω / V in Cu but with Ω^2 / V in Al-Mg-Si. We correlate this difference to the distinct interfacial contact states that are observed through *in situ* material flow characterization. In Cu, the interfacial contact between the material and tool head is characterized by a full slipping condition, so interfacial friction is the dominant heat generation mechanism. In Al-Mg-Si, the interfacial contact is characterized by a partial slipping/sticking condition, so both interfacial friction and plastic energy dissipation contribute significantly to the heat generation.

1. Introduction

While most metal additive manufacturing technologies to date have been based on selective melting and rapid solidification of powder or wire (i.e. beam-based additive technologies) [1–3], a series of *solid-state* metal additive manufacturing technologies have recently emerged that provide a low-energy pathway to achieve net-shaping or near-net-shaping with reduced heat input, thermal gradients, and residual stresses [4–6]. These solid-state technologies exploit deformation bonding to enable material adhesion via friction stir [7], ultrasonic vibration [8], or cold gas spraying [9]. The most recognized examples include additive friction stir deposition (AFSD) [10], friction stir additive manufacturing (FSAM) [11], ultrasonic additive manufacturing (UAM) [12], and cold spray [13]. By integrating the friction stir principle [14,15] with a robust material feeding mechanism [16], AFSD stands out as a free-form process allowing for site-specific deposition with good quality and properties in the as-printed state. Despite the large feature size resulting from the current tooling, AFSD has the potential for creating complex 3D geometries on a large-scale by properly machining the edges of the deposition tracks. FSAM and UAM are hybrid sheet-lamination technologies that require additional subtractive processes for shaping newly bonded layers. Cold spray enables site-specific deposition but generally requires post-processing to improve mechanical properties. With the unique benefits, AFSD has drawn great attention in the fields of multi-material additive manufacturing [17–20], selective-area coating and cladding [21], and additive repair [22].

In AFSD, a solid-state feed-rod is delivered through a hollow tool head as shown in Fig. 1(a). The tool head and feed-rod assembly rapidly rotate at a rotation rate, Ω, of ~10^2–10^3 revolutions per minute (RPM). When the rotating feed-rod contacts the stationary substrate, the dynamic interaction at the material-substrate interface generates

* Corresponding author.
E-mail address: hangyu@vt.edu (H.Z. Yu).

https://doi.org/10.1016/j.addma.2020.101386
Received 19 April 2020; Received in revised form 8 June 2020; Accepted 10 June 2020
Available online 16 June 2020

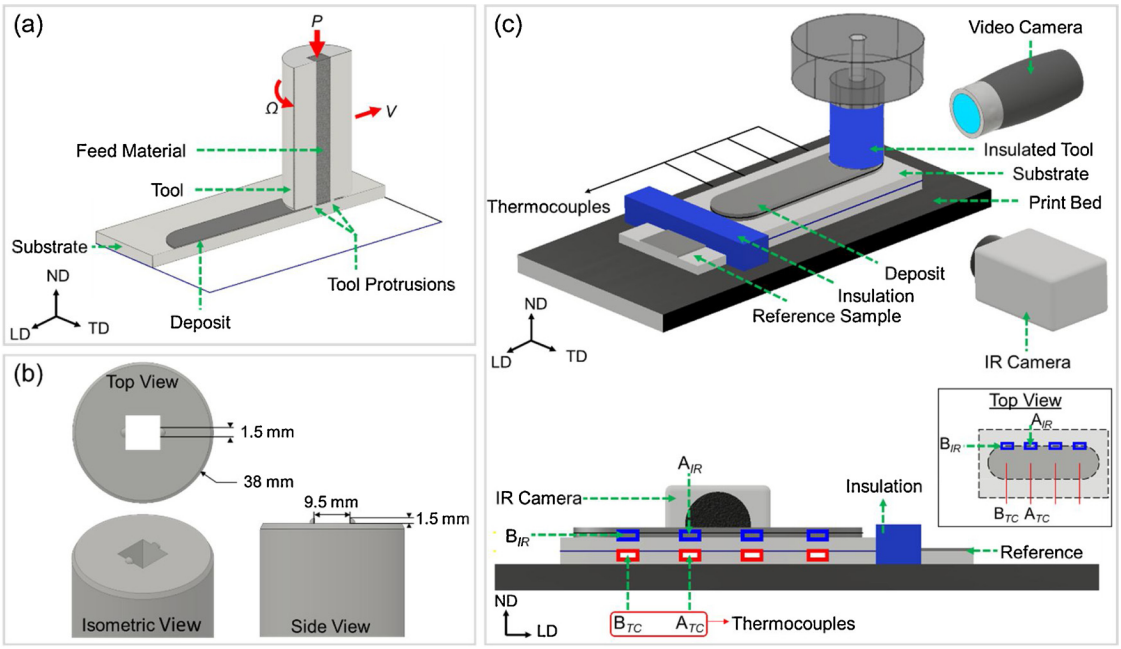

Fig. 1. An illustration of (a) the AFSD process, (b) the tool head including surface features and dimensions, and (c) the monitoring set-up. A_{TC} and B_{TC} are two locations in the substrate with the temperature measured by the thermocouples, whereas A_{IR} and B_{IR} are two locations in the first-layer of the deposited material with the temperature measured by the IR camera. A_{IR} and B_{IR} are directly above A_{TC} and B_{TC}. ND, TD, and LD refer to the normal direction, transverse direction, and longitudinal direction, respectively.

frictional heat, which in turn leads to thermal softening of the feed-rod. The combined compressive forces from the feeding apparatus and the shearing forces from the rotating tool head cause the feed-rod to plasticize and mix with the surface of the substrate. Rapid plastic deformation results in additional volumetric heat generation [23]. Furthermore, the tool surface features, such as protrusions, can generate additional frictional heat and enhance the material flow and mixing between the deposit and substrate. With co-deformation and mixing of the deposited material and substrate surface layers, in-plane motion of the substrate relative to the tool head leads to deposition of a single track of material with good interfacial bonding. During deposition, the material undergoes severe plastic deformation at elevated temperatures and high strain rates [24]. The accompanied continuous or discontinuous dynamic recrystallization gives rise to refined, equiaxed grains and excellent mechanical properties [6,10,21] in the as-printed state. This is a salient advantage as compared to conventional beam-based metal additive manufacturing processes, wherein the melting and solidification will result in cast-type microstructures featuring columnar and dendritic grains [25–28]. While these features can be avoided by controlling solidification via the introduction of nanoparticles [29] or very precise manipulation of transient thermal gradients [30], the associated efforts are time-consuming and expensive.

As in any metal additive manufacturing technology, the temperature evolution during AFSD controls the print quality, the microstructure, and the properties of the as-printed material. To investigate temperature evolution in AFSD, the distinctive consideration of *material flow* is necessary. On one hand, the material flow determines the volumetric energy produced from plastic deformation [31] and contributes to heat transfer via convective heat flow [32]. On the other hand, the material flow is influenced by the temperature distribution inside the deposited material, because the constitutive material properties —such as dynamic viscosity and flow stress — are strongly temperature dependent [33]. Therefore, as a friction stir-derived technology, the heat flow and material flow are fully coupled in AFSD.

Research of AFSD is at an early stage with a critical need for understanding the process fundamentals, especially the important thermal aspects. This necessitates direct experimental characterization of the *temperature evolution* and *material flow* during AFSD. For direct measurement of temperature evolution in the deposited material, AFSD shares many of the challenges as in friction stir welding (FSW) and friction stir processing (FSP) [34–36]. For example, thermocouples are challenging to embed within the processing zone because the large amounts of plastic deformation would likely destroy any physical sensors [37,38]. In addition, the tool in FSW, FSP, and AFSD obscures the stir zone or deposition zone, making it challenging to monitor the temperature evolution by top-view characterization (i.e., along the normal-direction). However, an important difference in AFSD is that the deposited material lies on top of the substrate, whereas in FSW or FSP the stir zone is internal to the workpiece material. Consequently, AFSD allows for direct measurement of the temperature evolution in the deposited material using non-contact methods from the *side view*, which can be implemented using infrared cameras or pyrometers [39,40]. For the same reason, the visualization of material flow is challenging in FSW and FSP; however, the surface of material flow can be directly monitored in AFSD from the side view.

The aim of this work is to gain physical insights into the process fundamentals of additive friction stir deposition via direct characterization of the temperature evolution, material flow, and heat generation mechanisms using *in situ* monitoring approaches. We employ infrared thermal imaging technology to monitor the temperature evolution in the deposited material from the side view and embed thermocouples in the substrate plate directly below the deposited material for complementary thermal measurements. Meanwhile, the material flow is monitored from the leading side of the deposit to provide valuable insights into the heat generation mechanisms. We investigate the deposition of two specific material systems, Cu and Al-Mg-Si, which are challenging to print using beam-based additive technologies due to the high thermal conductivity, high reflectivity, or susceptibility to hot cracking [41,42]. AFSD is a promising additive technology for Cu and Al-Mg-Si, because these materials are known to be well processed using the friction stir principle [32]. Cu and Al-Mg-Si differ in their thermo-mechanical responses; during forging Al-alloys undergo plastic flow more readily than Cu and Al-alloys are recognized for easier forgeability [43]. A comparative study of these two materials allows us to

explore the linkage between the thermomechanical properties of material and the consequential heat generation and thermal characteristics in AFSD.

2. Experimental procedures

2.1. Material deposition

All AFSD experiments were performed using a MELD R2 system (MELD Manufacturing Corporation, Christiansburg VA, USA) and a 38 mm-wide steel tool head. The tool surface had two protrusions with rounded surfaces and a height of 1.5 mm located immediately surrounding the feed-rod exit hole (see Fig. 1(b)). The build geometry of each experiment was a stack of two deposited layers with single-layer thickness of approximately 0.8 mm and a nominal length of 70.2 mm. Two different material systems were studied: (1) Cu (commercially pure), and (2) a commercially available Al-Mg-Si alloy, AA 6061. In both cases, the substrate and the deposited material had the same composition. Substrate plates were 6.35 mm × 76.2 mm × 127 mm. Raw feed material was in the form of square rod with a side length of 9.5 mm. Depositions were systematically performed at various AFSD processing conditions. The selected tool rotation rates included 300 RPM, 600 RPM, and 900 RPM, and the selected in-plane tool velocities included 1.00 mm/s, 2.00 mm/s, and 3.00 mm/s. The ratio between the material feed rate to the tool in-plane velocity was used to control the volumetric deposition rate, and kept constant throughout all experiments at a value of 1:3.

2.2. Thermal measurement

In this work, thermographic measurements were performed using a Micro-Epsilon TIM 400 infrared (IR) camera, which was mounted onto the bed of the AFSD system and shared the same reference frame as the print geometry. Temperature calibration of the IR camera was performed using AFSD-printed Cu and Al-Mg-Si samples, which were heated using a Fisher Scientific Hot-Plate under ambient conditions. By matching the IR outputs with the readings from a pre-calibrated thermocouple, the emittance for a given material (Cu or Al-Mg-Si) was calibrated [44,45]. This procedure was repeated at 50 K increments. To minimize IR measurement interference, additional modifications were made to the typical AFSD setup: the rotating tool and the spindle were both covered with fiberglass insulation to prevent undesirable radiative interference (e.g., reflections). During AFSD, a piece of Cu or Al-Mg-Si kept at known elevated temperatures was placed in the camera field of view to serve as a temperature reference. The IR camera had a capture rate of 80 Hz with 382 × 288 pixels in the field of view. The IR camera was positioned perpendicular to the side of the deposit at a distance of 11 cm. The pixel size provided sufficient resolution to distinctly measure the temperature of each layer while still providing a large field of view to capture the entire length of the deposit.

In addition to IR thermal measurement, a thermocouple array (K-type) was employed to continuously measure local temperatures in the substrate directly beneath the deposited material. Shallow grooves for thermocouple leads were cut into a second substrate plate, which was clamped underneath the primary substrate. Each groove was filled with a conductive thermal paste to improve the contact conditions and response time. Thermocouple data-logging was accomplished using Adafruit thermocouple amplifiers and an Arduino Nano microcontroller.

2.3. Monitoring of material flow

Optical video recording of the material flow was performed on the leading edge of the deposit using a Dino-Lite Edge AM4115ZT Microscope. The camera had a spatial resolution of 1280 × 1024 pixels with a pixel size of 0.03 mm × 0.03 mm at the given field of view. The optical camera was positioned perpendicular to the leading edge of the deposit at a distance of 8 cm. A high-temperature black primer was speckled onto the surface of the deposit during AFSD, in order to track the motion of the material relative to the tool head. The black speckles provided contrast on the surface of the deposited material and were individually tracked to monitor the motion of the deposited material. Comparison of the velocity of the speckles to the tool head rotation provided valuable insights into the stick-slip phenomena in each material system. Fig. 1(c) schematically shows how the infrared thermal imaging, thermocouple measurement, and optical video recording are incorporated into the present AFSD system.

3. *In situ* characterization of temperature evolution during AFSD of Cu and Al-Mg-Si

3.1. Qualitative overview of thermal field evolution in AFSD

AFSD is composed of three distinct processing phases (1) plunge, (2) in-plane motion, and (3) out-of-plane layer transition. In the plunge phase, the rotating feed-rod is slowly pushed downward through the center of the tool head by the feeding apparatus so that it makes contact with the stationary substrate. Initially, heat is generated by Coulomb friction at the feed-rod and substrate interface until the material has substantially softened and begins to plasticize. During plasticization, the majority of the plastic work is converted to heat, resulting in an additional volumetric heat generation mechanism. The continuously plasticizing material extrudes radially until the space beneath the rotating tool is saturated. The in-plane motion phase then begins, where the substrate is set in motion relative to the rotating tool; as a result, material is continuously deposited onto the substrate. Once the desired geometry has been traced by the in-plane motion and a layer is complete, the out-of-plane layer transition phase begins, in which the print bed lowers in the out-of-plane direction by the desired layer thickness.

An overview of the measured thermal field evolution during these phases is shown in Figs. 2 (a)-(f), which consist of several representative snapshots from a thermal video for a two-layer Cu deposition. The complete thermal video is available in the *Supplemental Information*. Time step $t = 0$ s corresponds to the thermal profile of the plunge phase. The in-plane motion phase is seen at $t = 25$ s where the print bed translates relative to the rotating tool. The track behind the tool head remains at an elevated temperature as it cools down through boundary heat losses (conduction, convection, and radiation). At $t = 35$ s, the layer transition begins. At $t = 55$ s, the second layer is being deposited, where the relative motion between the print bed and the tool is in the opposite direction to the first layer of deposition. At $t = 75$ s, the desired two-layer geometry is complete, and the print bed is lowered as the feed-rod detaches from the deposit. The final thermal image shows a bowl-shaped high temperature zone surrounding the end of deposition, which corresponds to the expected temperature distribution resulting from a moving heat source [46].

Based on the temperature measurement at a given spot, typical temperature evolution history (i.e., *T-t* plot) of the deposited material is shown in Fig. 2(g), showing two distinct peaks. The first peak corresponds to the deposition of new material at Spot A_{IR} (see Fig. 1(c) for the location), T_{Peak}. This is an intrinsic thermal characteristic depending on the AFSD processing parameters and tool-material interactions. The heating portion in the first peak is not physically meaningful because no material is initially present in the field of view. The measured 'heating rate' mostly reflects the IR camera response time rather than the temperature increase rate in the deposited material. The second peak corresponds to deposition of the second layer directly above Spot A_{IR}, clearly showing a strong reheating effect between layers in AFSD. The value of the second temperature peak depends on the print geometry, tool path, and the transition time between deposition of the first and second layer, so it is not an intrinsic thermal characteristic in AFSD. We note that the flat curve seen at ~450 K results from the limits of the

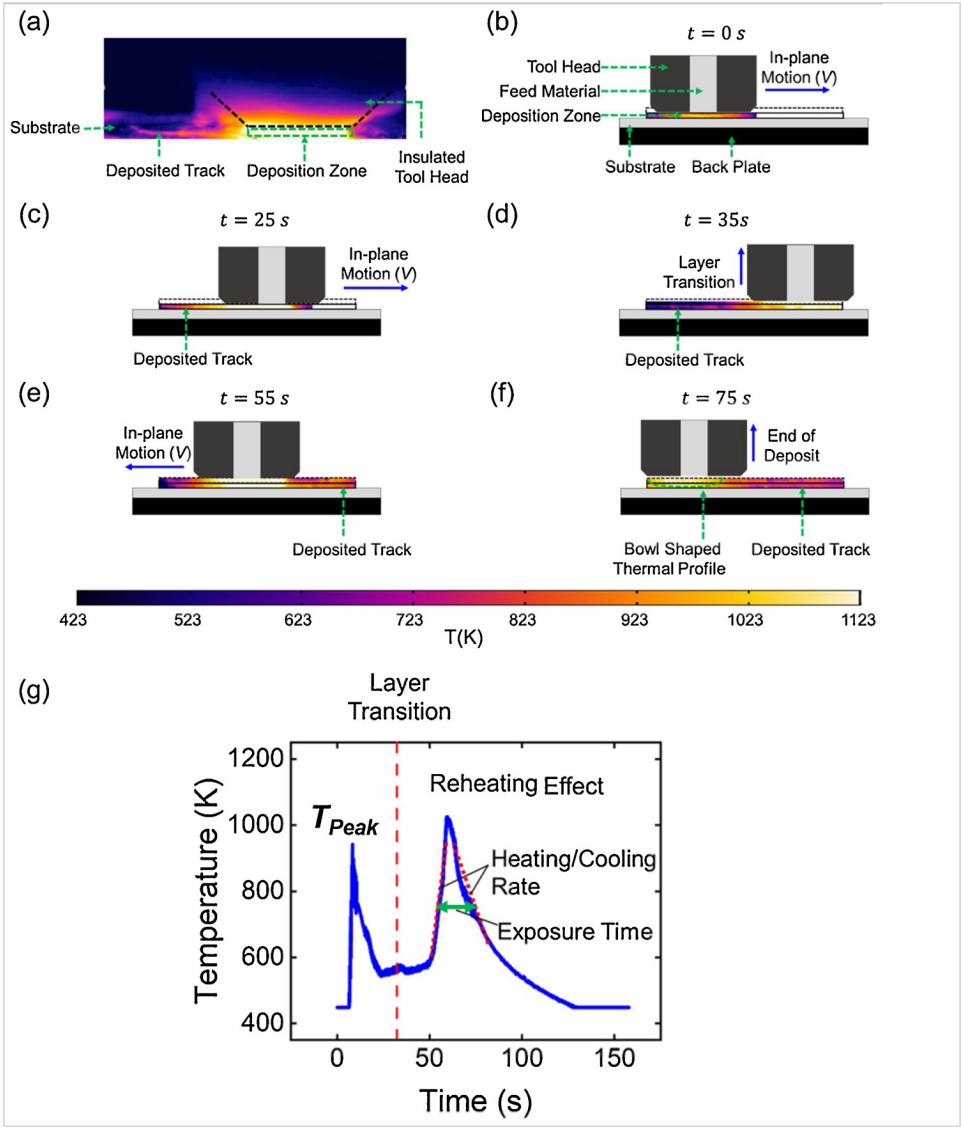

Fig. 2. An overview of the thermal profile for Cu deposited at 600 RPM and 1 mm/s in-plane velocity. (a) A representative thermal image of the entire field of view during AFSD. (b)-(f) The different time steps show the measured temperature field directly beneath the tool head, cooling of the deposited material at the far-from-the-tool position, and a bowl-shaped heat profile associated with a moving heat source. (g) A plot of the temperature history measured for a single spot of the deposit that demonstrates a temperature peak due to deposition and a substantial reheating effect.

measurable temperature range by the IR camera.

3.2. Dependence of peak temperature on AFSD processing conditions

The temperature field evolution has been systematically investigated for various AFSD processing conditions. For all successful Cu depositions without apparent defects in this work, the peak temperature T_{Peak} lies in the range of 49%–79% of the melting temperature T_M. For all successful Al-Mg-Si depositions, T_{Peak} lies in the range of 76%–92% of T_M. This is consistent with the fact that the yield strength of Cu drops more rapidly than structural Al alloys as temperature increases [47,48], so Cu can be friction stirred at a lower homologous temperature [49].

For both Cu and Al-Mg-Si, we study the trend of the peak temperature T_{Peak} with respect to the AFSD processing parameters, such as the tool head rotation rate Ω and in-plane velocity V. As plotted in Fig. 3, T_{Peak} shows a strong dependence on AFSD processing conditions, with Cu and Al-Mg-Si exhibiting similar trends. For a given tool rotation rate, it is observed that T_{Peak} decreases with increasing the tool in-plane velocity V. For a given V, T_{Peak} increases with increasing Ω. This trend is similar to that observed in FSW literature [50–53], which can be explained as follows: an increase of the tool rotation rate Ω is expected to increase the heat generation rate resulting from friction at the material-tool head interface, which leads to a positive correlation between T_{Peak} and Ω. With a higher in-plane velocity V, the material feed rate is higher and more material is deposited for a given period of time, so the heat input is lower per unit material volume. This leads to a negative correlation between T_{Peak} and V.

Quantitatively, we find that the peak temperature in AFSD is well described by power law relationships with the processing parameters. Arbegast has proposed an empirical power law equation of the peak temperature in FSW of Al alloys [54]: $T_{Peak}/T_M = K(\Omega^2/V)^a$, where K and a are fitting constants and Ω^2/V is a pseudo-heat index described by the key processing parameters. Using this type of relationship, the fitting results of the measured AFSD peak temperature are shown in Fig. 4(a) and Fig. 4(b) for Cu and Al-Mg-Si, respectively. The peak temperature in Al-Mg-Si is well predicted by the heat index of Ω^2/V with an R-squared value of 0.98 in the ln-ln plot. For Cu, the fitting is relatively poor with an R-squared value of 0.81. Fig. 4 (c) and Fig. 4(d) plot the fitting results of peak temperature using a pseudo-heat index of Ω/V instead, i.e., $T_{Peak}/T_M = K(\Omega/V)^a$, showing a good fit of the Cu

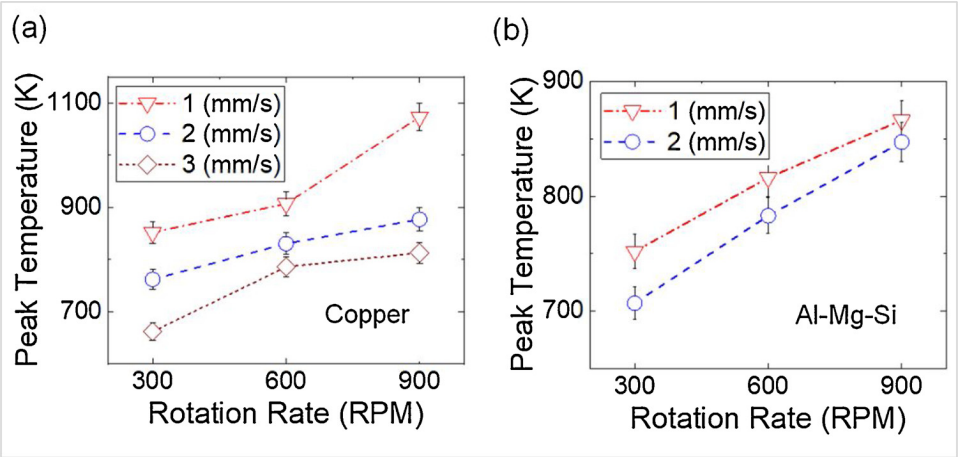

Fig. 3. Plots showing the peak temperature measured during deposition of the first layer at various processing conditions for (a) Cu and (b) Al-Mg-Si. In general, processing conditions with lower velocity and higher rotation rate produce higher peak temperatures. Error bars signify expected measurement error from the IR camera.

peak temperature with an R-squared value of 0.95 in the ln-ln plot. In contrast, the Al-Mg-Si peak temperature does not fit well with an R-squared value of 0.87. Therefore, the peak temperature in Cu forms a power law relationship with Ω/V, whereas the peak temperature in Al-Mg-Si forms a power law relationship with Ω^2/V.

Based on the fitting results in Fig. 4, the peak temperature of Cu and Al-Mg-Si during AFSD is best described by Eq.s 1 and 2, respectively:

$$\frac{T_{Peak}}{T_M} = K_{Cu}\left(\frac{\Omega}{V}\right)^{0.2}, \text{ for Cu.} \tag{1}$$

$$\frac{T_{Peak}}{T_M} = K_{Al}\left(\frac{\Omega^2}{V}\right)^{0.07}, \text{ for Al– Mg– Si.} \tag{2}$$

Here, K_{Cu} and K_{Al} are constant. In Arbegast's empirical fitting, the power a is found to be in the range of 0.04 to 0.06 for FSW of Al alloys. To compare, Eq. (2) shows a comparable power value of 0.07 in AFSD of Al-Mg-Si, suggesting similar heat generation mechanisms in AFSD and FSW of Al alloys. For Cu, however, the peak temperature exhibits a power law relationship with Ω/V rather than Ω^2/V, suggesting differences in the heat generation mechanisms. We correlate this finding to the distinct interfacial contact states and material flow behaviors between Cu and Al-Mg-Si, which will be elaborated in Sections 4 and 5. We note that the goal of fitting here is to show the different temperature evolution behavior between Cu and Al-Mg-Si; the latter is much more consistent with the Abergast model than the former. The intent is not to determine the exact fitting constants in the power laws, which may be challenging to achieve based on the limited data points in Fig. 4.

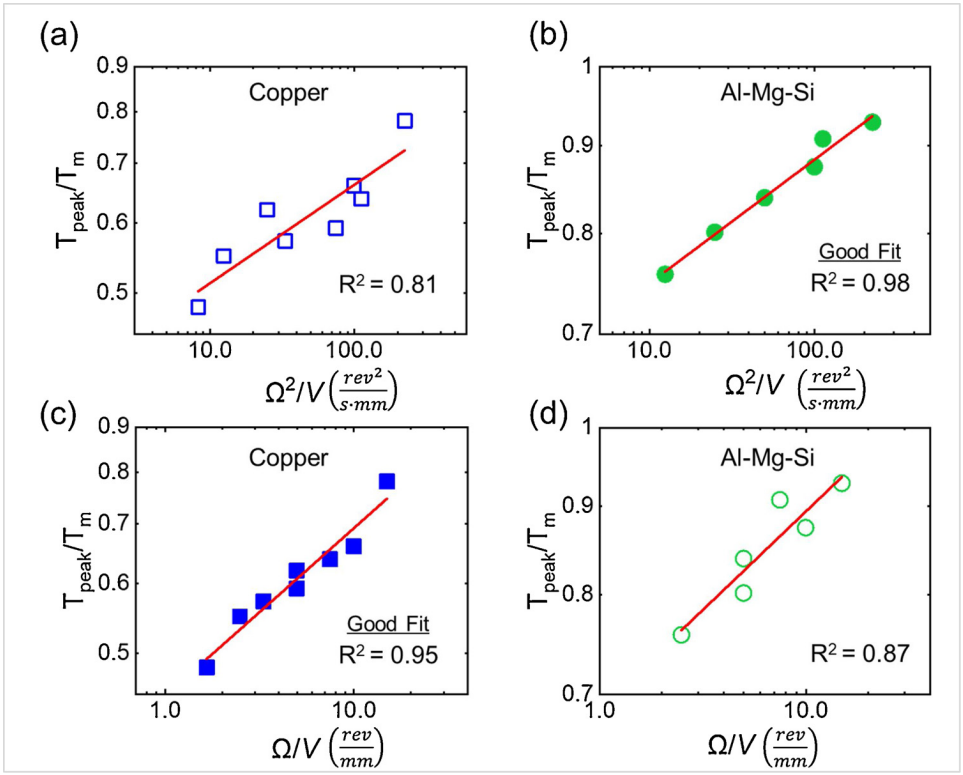

Fig. 4. Fitting of a power law relationship to the homologous peak temperature and the processing parameters with a relationship of (a, b) Ω^2/V and (c, d) Ω/V. Here, resolution per second (rev/s) is used as the unit for Ω and millimeter per second (mm/s) is used as the unit for V. The peak temperature for Cu shows a better fitting with Ω/V, whereas Al-Mg-Si has a better fitting with Ω^2/V.

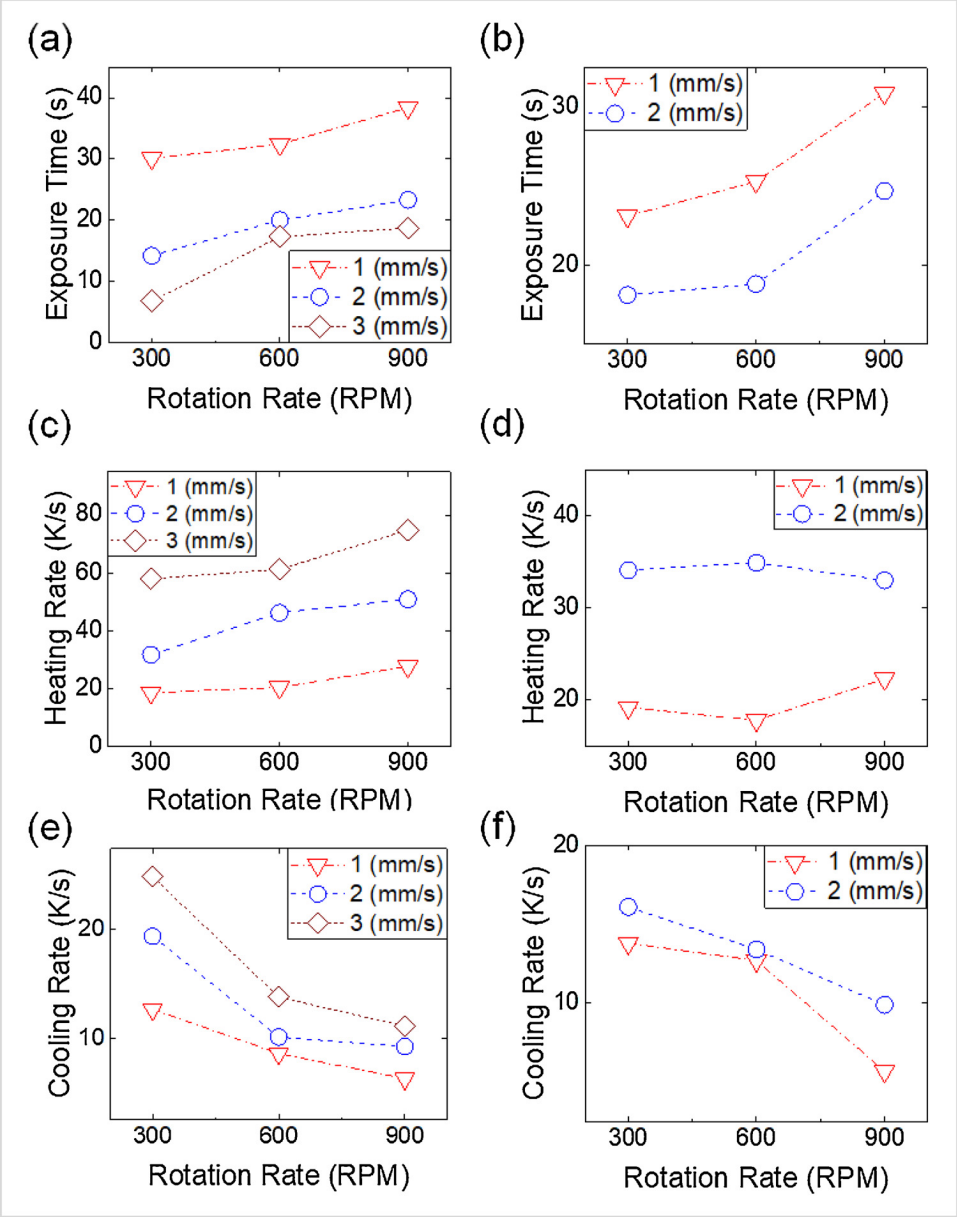

Fig. 5. Plots of (a, b) the exposure time, (c, d) the heating rate, and (e, f) the cooling rate as a function of the AFSD processing parameters. The left column corresponds to the data of Cu and the right column corresponds to Al-Mg-Si. Generally, the exposure time increases with increasing Ω and decreasing V, the heating rate increases with increasing V, and the cooling rate increases with decreasing Ω and increasing V.

3.3. Trends of exposure time, heating rate, and cooling rate

In addition to peak temperature, other important thermal characteristics include the exposure time, heating rate, and cooling rate, which can be conveniently extracted from the *T-t* plot (e.g., see Fig. 2 (g)). The goal here is to understand how these thermal characteristics change with respect to the AFSD processing parameters. We estimate the exposure time and heating rate based on the second peak in the *T-t* plot, because the heating portion of the first peak only reflects the response time of IR camera as explained in section 3.1. As such, this essentially measures the reheating effect arising from the deposition of a new layer. We estimate the cooling rate based on both the first and the second peak in the *T-t* plot, which are found to have the same trend with respect to the AFSD processing parameters.

The exposure time is the length of time that the deposited material experiences high temperatures, which is experimentally determined by finding the full width at half maximum of the peak temperature in the $T-t$ plot. Figs. 5(a) and (b) clearly show that the exposure time decreases with an increase of V. This trend can be explained by considering the positive correlation between the exposure time and the time of material interaction with the tool head. The latter can be roughly estimated as the ratio between the deposition radius and the tool in-plane velocity, and will decrease with an increase of V. As a result, the exposure time also decreases with an increase of V as seen in Figs. 5(a) and (b). The exposure time increases with the tool head rotation rate Ω as concluded from the same plots. This trend is expected because a higher rotation rate Ω leads to a higher peak temperature (when the in-plane velocity remains constant). It generally takes more time to cool down from a higher peak temperature, so the exposure time is longer.

The instantaneous heating and cooling rates are time dependent. From an engineering perspective, we define the average heating and cooling rates based on linear regions of the second peak in the $T-t$ plot. This is associated with a wide temperature range with respect to

T_{Peak}. In this work, the lower bound of the temperature range is set to be 30 % above the lowest measurable temperature of the IR camera (~600 K for Cu and ~500 K for Al-Mg-Si). With this setting, the interference from the first temperature peak can be avoided and good linear fitting can be achieved in the $T-t$ plot. The slope of the linear fitting (in absolute value) is used as the heating or cooling rate. Figs. 5(c) and (d) plot the heating rate under various AFSD processing conditions, which is generally in the range of 20–80 K/s. At a high in-plane velocity V, the heat source quickly approaches a given point and results in a rapid transition from the idle temperature to the peak temperature. Thus, the heating rate shows a positive correlation with the tool velocity V. Figs. 5(e) and (f) plot the trends of the cooling rate, which is measured to be in the range of 5–25 K/s. For both Cu and Al-Mg-Si, lower cooling rates are found to occur at higher Ω and lower V, which corresponds to conditions with higher peak temperature and more total heat input. This trend can be explained as follows: under conditions of high Ω and low V, the heat input is large, and significant preheating occurs in the substrate material ahead of the moving tool head. As a result, the local temperature gradient ∇T is reduced across the newly deposited material and the substrate below, leading to a lower cooling rate—as long as the thermal conduction into the substrate is a major cooling mechanism. This is confirmed in the Appendix, in which we study the substrate temperature evolution and evaluate the contribution of different cooling mechanisms during AFSD of Cu and Al-Mg-Si, including thermal conduction, air convection, and radiation.

4. *In situ* characterization of material flow during AFSD of Cu and Al-Mg-Si

From the *in situ*thermal characterization results in Section 3, we conclude that the key thermal characteristics, such as exposure time, heating rate, and cooling rate, exhibit similar trends with respect to the AFSD processing parameters in Cu and Al-Mg-Si. These trends can be explained by linking the heat generation and thermal transfer processes to the tool head rotation rate and in-plane velocity in a qualitative manner. However, there is a salient, quantitative difference between Cu and Al-Mg-Si (as shown in Section 3.2): the peak temperature exhibits a different power law relationship with the processing parameters for each material system. Such a quantitative difference in peak temperature cannot be understood without delving into the material flow behavior, because the heat flow is fully coupled with material flow in AFSD.

4.1. Fundamentals of material flow and interface contact in AFSD

AFSD begins with a solid, square feed-rod that is in contact with the substrate but not in contact with the bottom surface of the tool head. For the convenience of description, the following discussion treats it as a cylindrical rod with an equivalent surface area and a starting radius R_0. A compressive force is applied to the feed material as it rotates with the tool head (Fig. 6(a)). With the heat generation at the material-substrate interface, the feed material raises temperature and extrudes underneath the tool head (Fig. 6(b)). This involves a macroscopic material shape change via plastic deformation [55]. The new material is constrained vertically by the substrate and tool head, so it fills space with a thickness h pre-defined by the gap between the tool head and the substrate. The steady-state configuration is shown in Fig. 6(c). For the transverse cross-section of the deposition track, we refer to the region directly below the feed-rod as the *transition zone* (radius of R_0), where the feed material transitions from a compression-dominated state in the solid feed-rod to a shear-dominated state below the rotating tool head. We refer to the region vertically constrained by the tool head and the substrate as the *deposition zone*, which has a radius ranging from R_0 to R. The outer radius of the transition zone in AFSD is analogous to the pin edges in FSW. However, there is no sharp interface between the transition zone and the deposition zone in AFSD like that between the pin and workpieces in FSW because the transition zone and deposition zone are occupied by the same material.

In the steady state of AFSD, heat can be generated by the interfacial friction caused by slipping of the tool head on the deposited material. The interfacial heat generation rate Q_δ is a function of the interfacial contact stress $\tau_{contact}$ and the velocity difference between the tool head and the top surface of the deposit. The latter can be written as $\Delta v\,(r) = r\Omega - (1-\delta)r\Omega = \delta(r)r\Omega$ [56], where r is the radial position denoting the distance to the central rotating axis. $\delta(r)$ is the fractional slip and $(1-\delta(r))$ is the sticking coefficient. The linear velocity of the tool head increases along the radial direction, and it is harder for the deposited material to keep the same rotation rate as the tool head. Thus, we expect a decrease of the sticking coefficient with an increase of r, which is illustrated in Fig. 6(d). In addition to slipping, it is possible to have the sticking condition dominate at the tool-material interface, especially at small r values [57]. This corresponds to the scenario where material in the deposition zone rotates together with the tool head, rendering a volume of material with intensive flow. The material velocity gradient in this volume results in shear deformation and plastic energy dissipation, with the corresponding volumetric heat generation rate Q_V depending on the shear strain rate and the shear stress at yielding [58].

Overall, the heat generation in AFSD critically depends on the contact state at the tool-deposit interface and the volume of material flow. These two features are challenging to experimentally measure in FSW, because the stir zone in the workpieces is completely covered by the tool head. However, they can be explored via side-view monitoring in the AFSD configuration since the deposited material lies on top of the substrate.

4.2. Distinct material flow behaviors and contact states observed in Cu and Al-Mg-Si

To explore the material flow and tool-deposit contact state, we have monitored the leading edge of the deposit using an optical camera and found drastically different behavior between AFSD of Cu and Al-Mg-Si. The first notable difference is the footprint of the deposition track. As illustrated in Figs. 7(a) and (b), in Cu, the deposited material does not significantly extend toward the leading direction. The leading edge of the Cu deposit is only slightly ahead of the leading edge of the feed-rod. In contrast, in Al-Mg-Si, the deposited material extends significantly toward the leading direction. For Cu, *in situ* monitoring from the leading side can provide the material flow and rotation information inside the deposition zone—almost reaching the transition zone. For Al-Mg-Si, however, the monitoring can only capture the exterior surface of the deposition zone.

The second notable difference lies in the contact state of the tool-material interface in the deposition zone. Cu is found to remain effectively stationary after being extruded into the deposition zone, so the tool-material interface is characterized by a full slipping condition. In contrast, the exterior surface of Al-Mg-Si is seen to rotate with the tool head, although at a much lower rate, suggesting a partial slipping/sticking condition at the tool-material interface. Figs. 7(c) and (d) show snapshots of the optical videos captured on the leading edge, wherein the flow paths of two distinct spots on the deposit surface are investigated for each material system. There is a balance of the camera spatial resolution and time resolution to capture the important data for both material systems. In snapshot format, the movement of surface features may not be immediately evident due to lighting and contrast, so the videos are made readily available in the *Supplemental Information*.

In Cu (Fig. 7(c)), Spot M, which is below the tool head ($r \approx 1.5R_0$ but $r<R$), remains effectively stationary and does not follow the motion of the tool head rotation. In other words, $\delta = 1$ and the sticking coefficient is 0. Spot N is inside the deposition zone almost reaching the transition zone ($r \approx 1.1R_0$), and it is seen to move from the left to the far right in 0.13 s. Given the radius for the outer edge of motion and the time

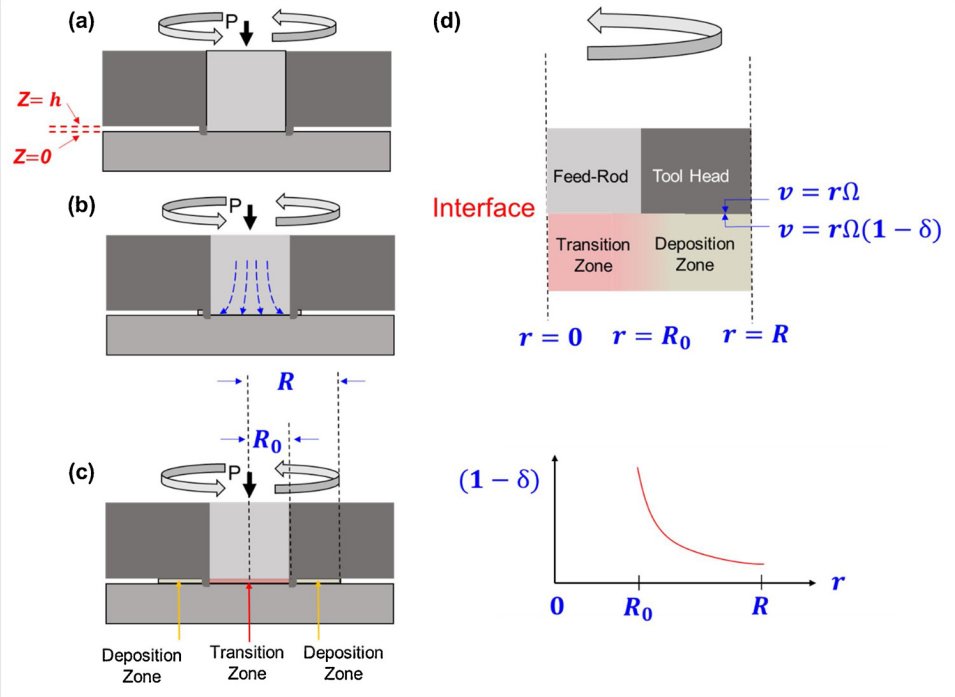

Fig. 6. A schematic of the AFSD process: (a) The initial plunge phase, (b) material extrusion while rotating, and (c) the steady-state stage where the deposited material occupies the transition zone directly below the feed-rod and the deposition zone below the tool head. (d) An illustration of the interface region, considering the velocity of tool head and material as well as the sticking coefficient.

between the snapshot images, we measure the linear velocity of Spot N to be 90 % of the tool head velocity at the same radius. In other words, for $r \approx 1.1R_0$, the sticking coefficient $(1-\delta)$ is 0.9 and $\delta = 0.1$. This observation shows that for Cu the material rotation and intensive flow are almost limited to the transition zone. At the boundary between the transition zone and deposition zone, the sticking coefficient rapidly drops from 0.9 to 0, and the fractional slip rapidly increases from 0.1 to 1. In the snapshots of Al-Mg-Si shown in Fig. 7(d), Speckle P and Q, which are both on the exterior surface of the deposition zone, move from left to right without observable changes in the relative distance over 1.51 s. The linear velocity of Spot P and Spot Q is measured as ~1% of the tool head velocity at the same radius. In other words, the sticking coefficient $(1-\delta)$ is 0.01 and $\delta = 0.99$. This observation suggests that material flow occurs throughout the entire deposit, from the transition zone to the edge of the deposition zone.

As shown in Fig. 6(d), we expect a decrease of the sticking coefficient along the radial direction for *both* Cu and Al-Mg-Si. However, there are significant differences between Cu and Al-Mg-Si based on the observation above:

- The sticking coefficient in Cu rapidly decreases to zero just outside of the transition zone, with a sharp transition of the material flow behavior across the boundary between the transition zone and deposition zone. Material rotation is almost absent in the deposition zone.
- The sticking coefficient in Al-Mg-Si shows a gradual decrease to non-zero values throughout the entire deposition zone ($R_0 < r < R$). The material rotation is observed even at the exterior surface of the deposition zone ($r = R$).

The evolution of the sticking coefficient along the radial direction observed in Cu and Al-Mg-Si is shown in Fig. 7(e).

Further insights into the material flow during AFSD can be gained by examining the flash forming at the edge of the deposition track, which shows visible differences between Cu and Al-Mg-Si. The top-view images in Figs. 8(a) and (b) show that the Cu flash develops discrete, sharp edges but the Al-Mg-Si flash is indistinguishable from the rest of the deposit. From the video snapshots in Fig. 7 (also see *Supplemental Information),* it is observed that the Cu flash begins to form as discontinuous sheets once the material enters the deposition zone. In the absence of material rotation, with more feed material extruded into the deposition zone, the previously-formed discontinuous sheets are pushed outward toward the edge of the tool head. In contrast, in Al-Mg-Si the entire deposition zone ($R_0 \leq r \leq R$) is observed to rotate with the tool head. As a result, the flash flows smoothly without geometric discontinuities. Such differences can be seen from the transverse cross-section images in Figs. 8(c) and (d).

5. Discussion

In Section 3, we show that the peak temperature T_{Peak} is correlated with Ω/V during AFSD of Cu but is correlated with Ω^2/V in Al-Mg-Si. This suggests that for peak temperature control, the relative dominance of tool rotation rate Ω over in-plane velocity V is stronger in Al-Mg-Si than in Cu. In Section 4, we show that the two materials have distinct interface contact states and material flow behaviors. In this section, we discuss the correlation between the two aspects in Sections 3 and 4 with an attempt to link the interface contact and material flow to the heat generation mechanisms in Cu and Al-Mg-Si.

5.1. Heat generation mechanisms: Cu vs. Al-Mg-Si

During AFSD of Cu, the material rotation and intensive material flow are mostly observed within the transition zone ($r < R_0$), whereas the majority of the material in the deposition zone ($R_0 < r < R$) does not rotate with the tool head. As a result, the volumetric heat generation is almost limited within the transition zone. Regarding the contact state at the tool-material interface, the deposition zone in Cu is characterized by a full slipping condition as the material appears to be largely stationary. This leads to significant interfacial heat generation by friction. During AFSD of Al-Mg-Si, even the exterior surface is found to rotate, suggesting that the material-tool head interaction effectively drives the material flow in the deposition zone. Therefore, significant shear deformation could occur after Al-Mg-Si is extruded beneath the tool head, resulting in considerable volumetric heat generation. Since the deposition zone in Al-Mg-Si is found to rotate with the tool head but at a lower rotation rate (see Fig. 7), the contact state is characterized by a partial slipping/sticking condition [59].

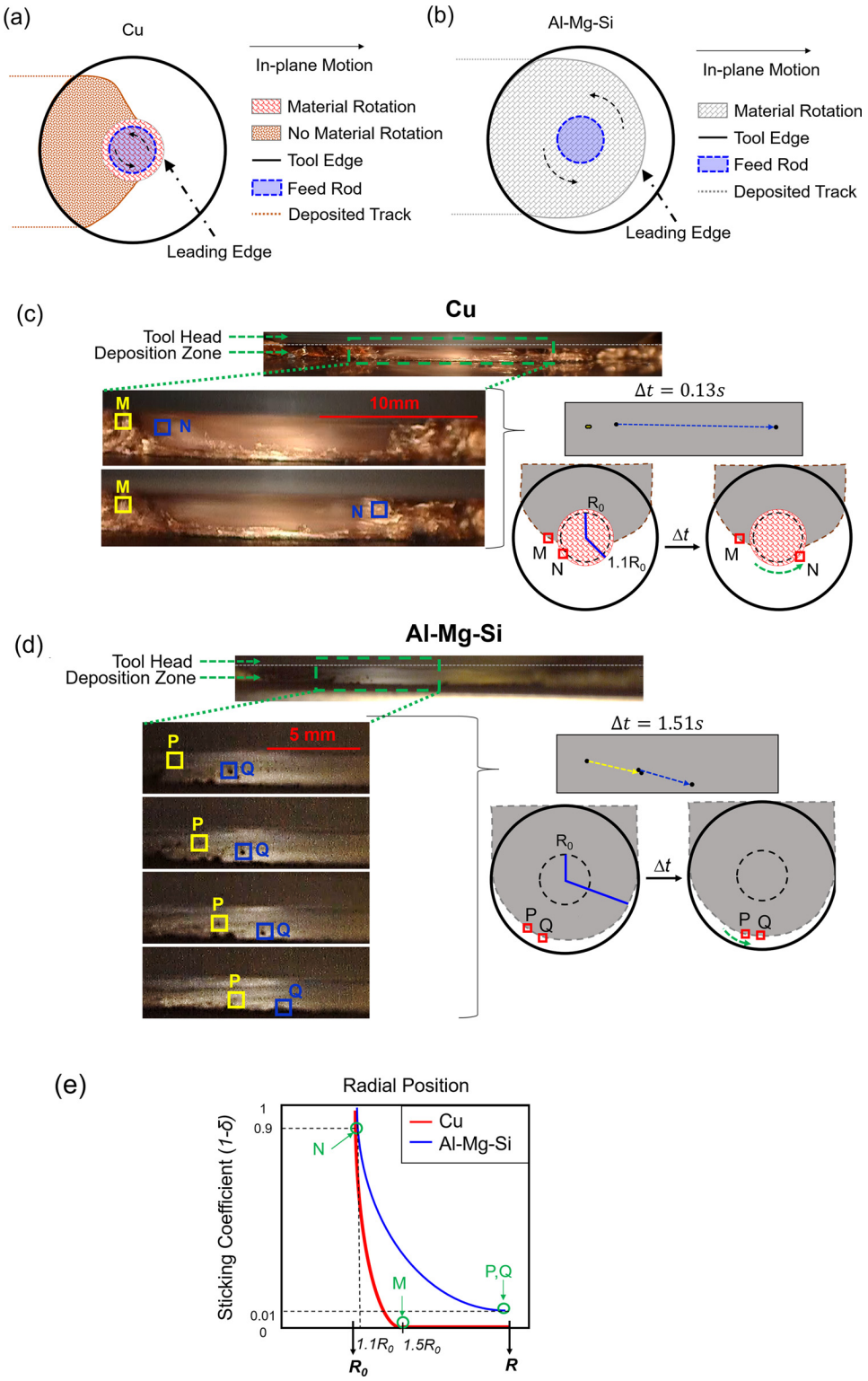

Fig. 7. The observed material flow features with the deposition footprint of (a) Cu and (b) Al-Mg-Si compared. Video snapshots of material flow are compared for (c) Cu and (d) Al-Mg-Si at 300 RPM and 2 mm/s in-plane velocity. The Cu snapshots show two distinct regions where Point M remains stationary and Point N rotates with the tool head; the Al-Mg-Si snapshots show the rotation of the entire deposition zone. (e) A schematic showing the differences between Cu and Al-Mg-Si in the observed sticking coefficient as a function of the radial position.

Because the deposition zone of Cu is characterized by slipping at the interface and minimal material flow, interfacial friction is expected to be the dominant heat generation mechanism for the deposition zone. For Al-Mg-Si, both the interfacial friction and volumetric energy dissipation from plastic deformation are important heat generation mechanisms. The differences in the heat generation mechanisms between Cu and Al-Mg-Si are illustrated in Fig. 9, in which the interfacial heat generation is marked by blue arrows and the volume of deposited material with significant volumetric heat generation is highlighted in red. We note that the color gradient of the figure corresponds to the

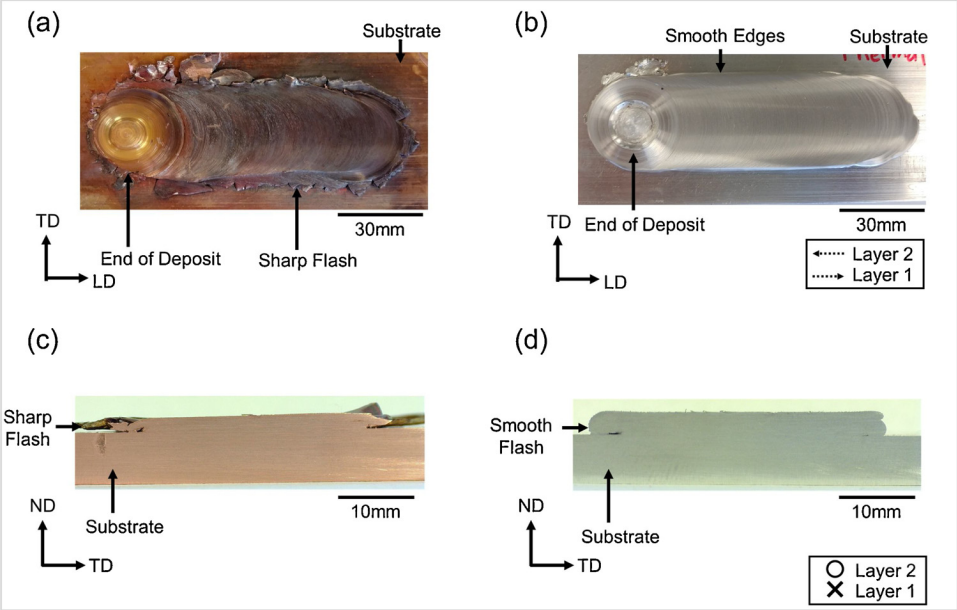

Fig. 8. Pictures of the as-deposited tracks for (a) Cu and (b) Al-Mg-Si from a top-down view. (c) and (d) show the transverse cross-section of Cu and Al-Mg-Si, respectively. A key difference between the two material systems is seen in the shape and continuity of the flash.

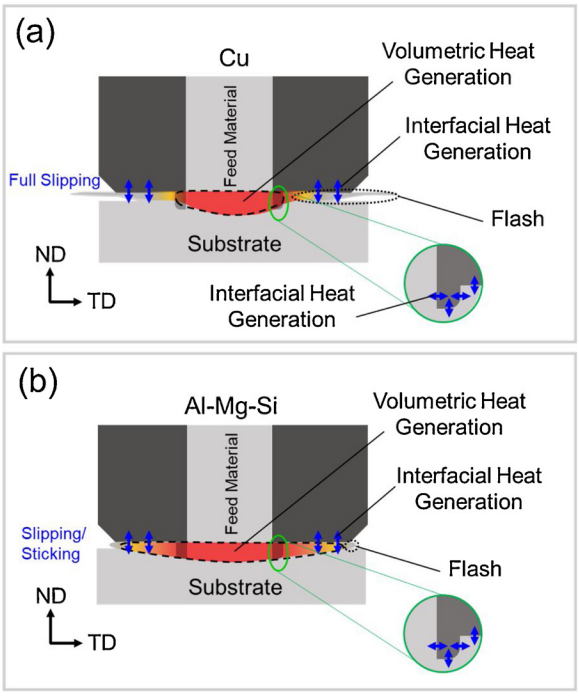

Fig. 9. A diagram showing the heat generation mechanisms for (a) Cu and (b) Al-Mg-Si. The volumetric heat generation regions are shown in red and the interfacial friction is highlighted with blue arrows. The Cu system has the most significant volumetric heat generation directly beneath the feed-rod. In Al-Mg-Si, the volumetric heat generation zone is large due to substantial material flow.

differences in material flow and rotation, rather than the temperature distribution. While more intensive material flow is expected in the transition zone, convection via material flow from the transition zone to the deposition zone could lead to higher temperatures in the deposition zone [60]. That being said, previous simulation works on FSW have predicted higher temperature in the center than the edge of the stir zone [56,61]. Determining the temperature distribution inside the transition zone and deposition zone in AFSD is beyond the scope of this work and will require future experimental or simulation efforts.

In addition to the frictional heat and plastic deformation driven by the stick-slip interface at the tool bottom surface, heat is generated due to the presence of tool protrusions. In this work, the tool protrusions height is 1.5 mm and the layer thickness is 0.8 mm. As a result, a significant portion of the protrusion penetrates into the substrate. The tool protrusions interact with the deposited material as well as the substrate, resulting in (i) frictional heating at the associated interfaces and (ii) substantial material flow in the volume surrounding the protrusion path. Regarding the amount of heat generation, the surface area of the protrusions is small ($\sim$10 mm^2) compared to the bottom surface of the tool head ($\sim$1140 mm^2), so the interfacial heat generation contributed by the protrusions is expected to be small globally. However, they locally raise the temperature and drive the material flow in the surface layers of the substrate, and thus play an important role in quality control in AFSD.

5.2. Influences of the tool head rotation rate on the heat generation mechanisms

Generally, the interfacial heat generation rate can be written as $Q_\delta = \int \tau_{contact}(v_{tool} - v_{material})d\widetilde{A} = \int \tau_{contact}(r\Omega)\delta d\widetilde{A}$, where $\tau_{contact}$ is the interfacial shear stress and $d\widetilde{A}$ is an infinitesimal interface area. The integration covers the entire deposition zone: $R_0 \leq r \leq R$. In AFSD of Al-Mg-Si, the fractional slip δ and the sticking coefficient $(1-\delta)$ vary for different r values in the deposition zone, so $Q_\delta^{Al-Mg-Si} = \int \tau_{contact}(r\Omega)\delta(r)d\widetilde{A}$. However, in AFSD of Cu, almost no material rotation is observed in the deposition zone, so δ is a constant at $\delta = 1$. Thus, the heat generation equation reduces to $Q_\delta^{Cu} = \int \tau_{contact}(r\Omega)d\widetilde{A}$. From these equations, the interfacial heat generation is expected to increase with the tool head rotation rate Ω in both Al-Mg-Si and Cu due to the term $r\Omega$. However, there is an additional term $\delta(r)$ in $Q_\delta^{Al-Mg-Si}$, which also increases with the rotation rate Ω. This is because an increase of Ω leads to an increase of the tool velocity, resulting in a decrease of the sticking coefficient and an increase of the fractional slip δ. Considering the appearance of Ω in both terms $r\Omega$ and $\delta(r, \Omega)$, it should have a more significant influence on the interfacial heat generation rate in Al-Mg-Si than in Cu.

The total volumetric heat generation rate can be written as $Q_V = \int \zeta \dot{\varepsilon}_{ij}^p \sigma_{ij} d\widetilde{V}$. Here $\dot{\varepsilon}_{ij}^p$ and σ_{ij} are the components of the plastic strain

rate tensor and the Cauchy stress tensor, the product of which defines the density of plastic energy dissipation [62]. ζ denotes the ratio of the heat converted from plastic deformation and ranges from 0.80 to 0.99 [63], $d\widetilde{V}$ is an infinitesimal volume, and the integration covers the volume of material with intensive flow. For Cu, the total volume of intensive flow $\widetilde{V}^{Flow}$ is almost equal to the volume of transition zone and is hardly influenced by the tool rotation rate. For Al-Mg-Si, $\widetilde{V}^{Flow}$ is larger than the volume of transition zone, and likely increases with the tool rotation rate Ω as suggested by previous studies. In FSW of Al alloy 7020-T6, Lorrain et al. [64] have experimentally observed an increase of the stir zone size with the tool rotation rate increasing from 300 RPM to 600 RPM. Using the methodology of scaling, Mendez et al. [65] have analyzed the heat transfer and plastic deformation during FSW and predicted a positive correlation between the thickness of the shear layer (volume with intensive flow) and the tool rotation rate. With $\widetilde{V}^{Flow}$ staying almost constant in Cu but increasing in Al-Mg-Si at a higher rotation rate, Ω should have a more significant influence on the volumetric heat generation rate in Al-Mg-Si than in Cu.

From these analyses, the tool head rotation rate Ω should have more influences on the interfacial and volumetric heat generation rates in Al-Mg-Si than that in Cu for a given in-plane velocity. This is probably the origin of the different power laws of peak temperature between Cu and Al-Mg-Si, wherein the relative dominance of tool rotation rate Ω over in-plane velocity V is found to be stronger in Al-Mg-Si than in Cu. Fundamentally, the drastically different contact states and material flow behaviors in Cu and Al-Mg-Si are related to stick-slip interactions with the tool head as well as their intrinsic thermomechanical properties. For solid materials, the sticking period between two surfaces is dependent on the kinetic friction coefficient between the interacting surfaces. Of particular importance here is the friction coefficients of the Fe-based tool and the deposited materials, Cu and Al. It is known that the kinetic friction coefficient between Cu:Fe is lower than Al:Fe [66,67], which leads to a lack of sticking in Cu to the rotating steel tool and a lower frictional shear stress. Beyond that, Al-Mg-Si has better intrinsic forgeability with easier plastic flow than Cu [43]. Even with the same contact shear stress, we would expect more intensive material flow and rotation in the deposition zone in Al-Mg-Si than in Cu.

6. Conclusions

In summary, we have investigated the temperature evolution and heat generation mechanisms during AFSD of Cu and Al-Mg-Si via *in situ* measurements of the thermal evolution and material flow. In addition to providing critical thermal data, this work has enabled quantification of the relationships between the AFSD processing conditions and key thermal characteristics, while providing physical insights into the differences in heat generation mechanisms between Cu and Al-Mg-Si. The most salient conclusions from this work include:

- T_{Peak} exhibits a power law relationship with Ω/V in Cu but with Ω^2/V in Al-Mg-Si.
- The exposure time, heating rate, and cooling rate for AFSD are approximately on the order of 10^1 s, 10^1 -10^2 K/s, and 10^1 K/s, respectively. The exposure time increases with an increase of Ω or a decrease of V, the heating rate increases with an increase of V, and the cooling rate increases with a decrease of Ω or an increase of V.
- During AFSD of Cu, material rotation primarily occurs in the material beneath the rotating feed-rod. The interface between the tool head and deposited material is under a full slipping condition, and interfacial friction is the dominant heat generation mechanism in the deposition zone. During AFSD of Al-Mg-Si, the tool rotation causes the material in the deposition zone to rotate. The interfacial contact is under a partial slipping/sticking condition. Both interfacial friction and volumetric energy dissipation contribute to the heat generation in the deposition zone.
- The differences in the heat generation mechanisms between Cu and Al-Mg-Si, which result from the distinct material flow behaviors and interface contact states, are likely to be the origin of their different power laws of peak temperature.

CRediT authorship contribution statement

David Garcia: Conceptualization, Data curation, Formal analysis, Writing - original draft. **W. Douglas Hartley:** Data curation, Formal analysis, Writing - review & editing. **Hunter A. Rauch:** Data curation, Formal analysis. **R. Joey Griffiths:** Formal analysis. **Rongxuan Wang:** Data curation. **Zhenyu J. Kong:** Conceptualization, Resources. **Yunhui Zhu:** Conceptualization, Formal analysis. **Hang Z. Yu:** Conceptualization, Formal analysis, Funding acquisition, Project administration, Writing - review & editing.

Declaration of Competing Interest

The authors declare that they have no known competing financial interests or personal relationships that could have appeared to influence the work reported in this paper.

Acknowledgements

The authors would like to thank the support from National Science Foundation (CMMI-1853893) as well as ICTAS at Virginia Tech through the Junior Faculty Award. The authors would also like to thank Mr. Andy Heller-Jones for assistance in experiments.

Appendix A. Substrate temperature evolution during AFSD

The IR camera provides important insight into the temperature distribution on the exterior surface of the deposited material. Complementary to that, the embedded thermocouples offer an accurate and reliable measurement of the substrate temperature directly beneath the deposited material. Fig. A1 shows the typical temperature evolution in Cu and Al-Mg-Si measured by thermocouples at positions A_{TC} and B_{TC}. The measured *T-t* plots are overlaid with the IR temperature measurements of the deposited material selected at spots A_{IR}, and B_{IR}, which correspond to the location directly above A_{TC} and B_{TC}, respectively. The exact locations of the measurement can be found in Fig. 1(c) in the main text.

The temperature evolution in the deposited material measured by IR imaging shows a sharper peak with a higher magnitude, a smaller exposure time, a higher heating rate, and a higher cooling rate compared to the temperature profile of the substrate measured by thermocouples. This is because the temperature measured by IR imaging results from the heat generation by tool-material interactions and possibly severe plastic deformation, whereas in the thermocouple data it is a result of the heat conduction from the deposited material into the substrate. Even before the arrival of the tool head at Point A_{IR}, Point A_{TC} in the substrate experiences a gradual pre-heating effect due to the material deposited (of elevated temperature) before Point A_{IR}. The preheating and gradual cooling from conduction result in a broader temperature profile than Point A_{IR}. The temperature profiles for each spot are strongly site-specific. Locations far from the layer transition, such as Spot A_{TC} and A_{IR}, experience two distinct peaks with substantial cooling between layers, as seen in Figs. A1 (a) and (b). Spot B_{TC} and B_{IR} are much closer to the layer transition, so the two peaks from each layer deposition are seen to overlap (see Figs. A1 (c) and (d)).

The difference in the measured temperature at Spot A_{IR} and A_{TC} or Spot B_{IR} and B_{TC} allows us to roughly estimate the contribution of cooling

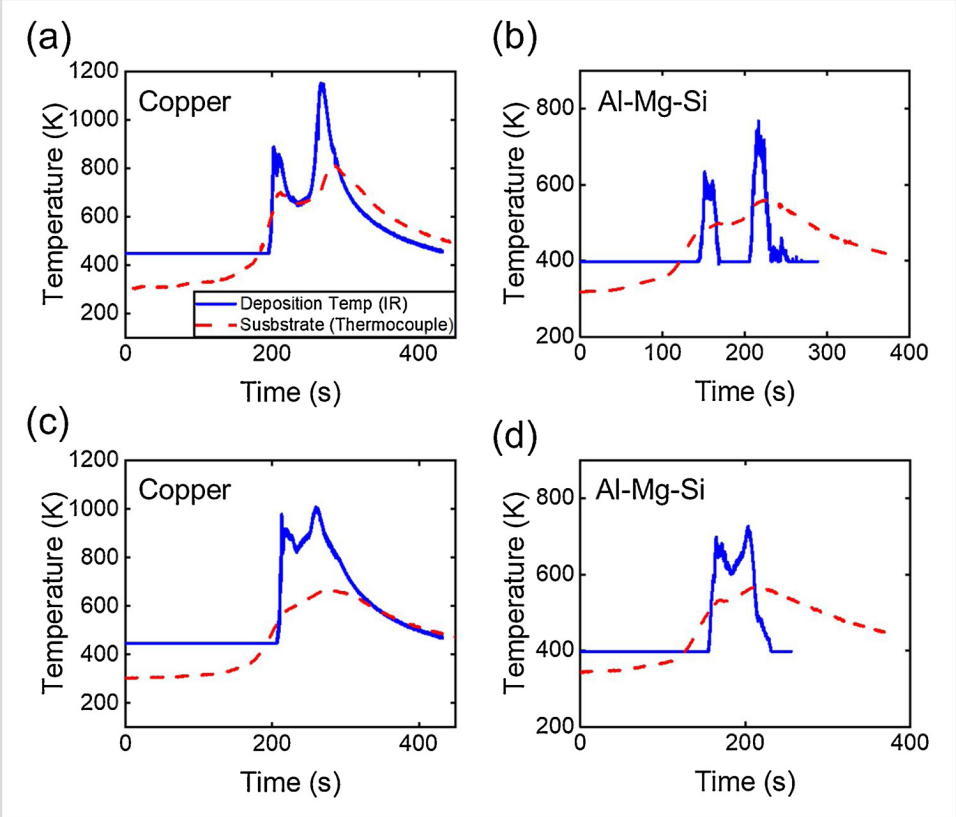

Fig. A1. Temperature-time plots of spot A_{TC} and A_{IR} for (a) Cu at 300 RPM and 1 mm/s in-plane velocity (b) Al-Mg-Si at 300 RPM and 2 mm/s in-plane velocity. Plots (c) and (d) correspond to the temperature-time plots of B_{TC} and B_{IR} for Cu and Al-Mg-Si, respectively. In general, the temperature curve measured by the IR camera shows a narrower peak with greater magnitude than the corresponding temperature of the substrate.

mechanisms in AFSD. We consider the heat flux by thermal conduction into the substrate, air convection, and radiation [51–53]. Heat flux by conduction can be estimated using Fourier's conduction law $\Phi_{conduction} = -\kappa \bullet {}^{\Delta T}/_{\Delta x}$, where κ is the thermal conductivity. ΔT is the difference in temperature between the deposited material (measured from the IR camera) and the substrate below it (measured from the embedded thermocouples), and Δx is the distance between the two measured locations. Using κ = 401 and 170 W/m•K for Cu and Al-Mg-Si respectively [68] as well as Δ x= 6.8×10^{-3}m (dimension measured in our experiment), $\Phi_{conduction}$ is calculated to be on the order of 10^7 W/m^2 or above for both materials. Heat flux of convection can be estimated using Newton's law of cooling $\Phi_{convection} = -h \bullet (T - T_{environment})$. Here, h is the heat transfer coefficient of air assumed to be in the range of 10 − 100 W/m^2•K [66], T is the peak temperature measured by the IR camera, and $T_{environment}$ is the ambient temperature set to be 298 K. With these numbers, $\Phi_{convection}$ is estimated to be $\sim$ 10^3-10^4 W/m^2. The heat flux by radiation is $\Phi_{radiation} = \varepsilon\sigma(T^4 - T^4_{environment})$, where the Stefan-Boltzmann constant $\sigma = 5.67\times10^{-8}$ W/m^2•K^4 and ε is the emissivity [68]. $\Phi_{radiation}$ is estimated to be $\sim$ 10^4 W/m^2. Apparently, the heat flux by conduction is much more significant than that by air convection and radiation. The total heat flow by each mechanism is a product of the heat flux and the cooling area. Considering the cooling area of each mechanism, the corresponding analysis concludes that conduction is the dominant cooling mechanism in AFSD for both Cu and Al-Mg-Si.

Appendix B. Supplementary data

Supplementary material related to this article can be found, in the online version, at doi:https://doi.org/10.1016/j.addma.2020.101386.

References

[1] I. Gibson, D. Rosen, B. Stucker, Directed Energy Deposition Processes, Additive Manufacturing Technologies: 3D Printing, Rapid Prototyping, and Direct Digital Manufacturing, Springer, New York, New York, NY, 2015, pp. 245–268.

[2] W.J. Sames, F.A. List, S. Pannala, R.R. Dehoff, S.S. Babu, The metallurgy and processing science of metal additive manufacturing, Int. Mater. Rev. 61 (5) (2016) 315–360.

[3] S.W. Williams, F. Martina, A.C. Addison, J. Ding, G. Pardal, P. Colegrove, Wire + arc additive manufacturing, Mater. Sci. Technol. 32 (7) (2016) 641–647.

[4] M. Norfolk, H. Johnson, Solid-state additive manufacturing for heat exchangers, JOM 67 (3) (2015) 655–659.

[5] W. Li, K. Yang, S. Yin, X. Yang, Y. Xu, R. Lupoi, Solid-state additive manufacturing and repairing by cold spraying: a review, J. Mater. Sci. Technol. 34 (3) (2018) 440–457.

[6] H.Z. Yu, M.E. Jones, G.W. Brady, R.J. Griffiths, D. Garcia, H.A. Rauch, C.D. Cox, N. Hardwick, Non-beam-based metal additive manufacturing enabled by additive friction stir deposition, Scr. Mater. 153 (2018) 122–130.

[7] G.K. Padhy, C.S. Wu, S. Gao, Friction stir based welding and processing technologies - processes, parameters, microstructures and applications: a review, J. Mater. Sci. Technol. 34 (1) (2018) 1–38.

[8] S. Krüger, G. Wagner, D. Eifler, Ultrasonic welding of Metal/Composite joints, Adv. Eng. Mater. 6 (2004) 157–159.

[9] S. Yin, P. Cavaliere, B. Aldwell, R. Jenkins, H. Liao, W. Li, R. Lupoi, Cold spray additive manufacturing and repair: fundamentals and applications, Addit. Manuf. 21 (2018) 628–650.

[10] O.G. Rivera, P.G. Allison, J.B. Jordon, O.L. Rodriguez, L.N. Brewer, Z. McClelland, W.R. Whittington, D. Francis, J. Su, R.L. Martens, N. Hardwick, Microstructures and mechanical behavior of Inconel 625 fabricated by solid-state additive manufacturing, Mater. Sci. Eng. A 694 (2017) 1–9.

[11] F. Khodabakhshi, A.P. Gerlich, Potentials and strategies of solid-state additive friction-stir manufacturing technology: a critical review, J. Manuf. Process. 36 (2018) 77–92.

[12] R.J. Friel, R.A. Harris, Ultrasonic additive manufacturing – a hybrid production process for novel functional products, Procedia Cirp 6 (2013) 35–40.

[13] A. Sova, S. Grigoriev, A. Okunkova, I. Smurov, Potential of cold gas dynamic spray as additive manufacturing technology, Int. J. Adv. Manuf. Technol. 69 (9) (2013) 2269–2278.

[14] M.K. Besharati-Givi, P. Asadi, Advances in Friction-Stir Welding and Processing, Elsevier Science, 2014.

[15] R.S. Mishra, Z.Y. Ma, Friction stir welding and processing, Mater. Sci. Eng. R Rep.

50 (1) (2005) 1–78.
[16] J.P. Schultz, K.D. Creehan, Fabrication Tools for Exerting Normal Forces on Feedstock, Aeroprobe Corporation, (2017).
[17] R.J. Griffiths, M. Perry, J. Sietins, Y. Zhu, N. Hardwick, C.D. Cox, H.A. Rauch, H.Z. Yu, A perspective on solid-state additive manufacturing of aluminum matrix composites using MELD, J. Mater. Eng. Perform. (2018).
[18] D. Garcia, Z. Wu, J.Y. Kim, H.Z. Yu, Y. Zhu, Heterogeneous materials design in additive manufacturing: model calibration and uncertainty-guided model selection, Addit. Manuf. 27 (2019) 61–71.
[19] H.Z. Yu, S.R. Cross, C.A. Schuh, Mesostructure optimization in multi-material additive manufacturing: a theoretical perspective, J. Mater. Sci. 52 (8) (2017) 4288–4298.
[20] D. Garcia, M.E. Jones, Y. Zhu, H.Z. Yu, Mesoscale design of heterogeneous material systems in multi-material additive manufacturing, J. Mater. Res. 33 (1) (2018) 58–67.
[21] B.J. Phillips, D.Z. Avery, T. Liu, O.L. Rodriguez, C.J.T. Mason, J.B. Jordon, L.N. Brewer, P.G. Allison, Microstructure-deformation relationship of additive friction stir-deposition Al–Mg–Si, Materialia 7 (2019) 100387.
[22] R.J. Griffiths, D.T. Petersen, D. Garcia, H.Z. Yu, Additive friction stir-enabled solid-state additive manufacturing for the repair of 7075 aluminum alloy, Appl. Sci. 9 (2019) 3486.
[23] M. Song, R. Kovacevic, Numerical and experimental study of the heat transfer process in friction stir welding, Proceedings of the Institution of Mechanical Engineers, Part B: Journal of Engineering Manufacture 217 (1) (2003) 73–85.
[24] R. Nandan, G.G. Roy, T. Debroy, Numerical simulation of three-dimensional heat transfer and plastic flow during friction stir welding, Metall. Mater. Trans. A 37 (4) (2006) 1247–1259.
[25] L.E. Criales, Y.M. Arısoy, B. Lane, S. Moylan, A. Donmez, T. Özel, Laser powder bed fusion of nickel alloy 625: experimental investigations of effects of process parameters on melt pool size and shape with spatter analysis, Int. J. Mach. Tools Manuf. 121 (2017) 22–36.
[26] P. Nie, O.A. Ojo, Z. Li, Numerical modeling of microstructure evolution during laser additive manufacturing of a nickel-based superalloy, Acta Mater. 77 (2014) 85–95.
[27] L. Thijs, F. Verhaeghe, T. Craeghs, J.V. Humbeeck, J.-P. Kruth, A study of the microstructural evolution during selective laser melting of Ti–6Al–4V, Acta Mater. 58 (9) (2010) 3303–3312.
[28] O. Zinovieva, A. Zinoviev, V. Ploshikhin, Three-dimensional modeling of the microstructure evolution during metal additive manufacturing, Comput. Mater. Sci. 141 (2018) 207–220.
[29] J.H. Martin, B.D. Yahata, J.M. Hundley, J.A. Mayer, T.A. Schaedler, T.M. Pollock, 3D printing of high-strength aluminium alloys, Nature 549 (7672) (2017) 365–369.
[30] R.R. Dehoff, M.M. Kirka, W.J. Sames, H. Bilheux, A.S. Tremsin, L.E. Lowe, S.S. Babu, Site specific control of crystallographic grain orientation through electron beam additive manufacturing, Mater. Sci. Technol. 31 (8) (2015) 931–938.
[31] M.Z.H. Khandkar, J. Khan, A.P. Reynolds, Prediction of Temperature Distribution and Thermal History During Friction Stir Welding: Input Torque Based Model, (2003).
[32] R.S. Mishra, P.S. De, N. Kumar, Friction Stir Welding and Processing: Science and Engineering, Springer International Publishing, 2014.
[33] P.B. Hirsch, D.H. Warrington, The flow stress of aluminium and copper at high temperatures, Philos. Mag. 6 (66) (1961) 735–768.
[34] M. Assidi, L. Fourment, S. Guerdoux, T. Nelson, Friction model for friction stir welding process simulation: calibrations from welding experiments, Int. J. Mach. Tools Manuf. 50 (2) (2010) 143–155.
[35] S. Swaminathan, K. Oh-Ishi, A.P. Zhilyaev, C.B. Fuller, B. London, M.W. Mahoney, T.R. McNelley, Peak stir zone temperatures during friction stir processing, Metall. Mater. Trans. A 41 (3) (2010) 631–640.
[36] W. Woo, Z. Feng, X.L. Wang, D.W. Brown, B. Clausen, K. An, H. Choo, C.R. Hubbard, S.A. David, In situ neutron diffraction measurements of temperature and stresses during friction stir welding of 6061-T6 aluminium alloy, Sci. Technol. Weld. Join. 12 (4) (2007) 298–303.
[37] A. Gerlich, G. Avramovic-Cingara, T.H. North, Stir zone microstructure and strain rate during Al 7075-T6 friction stir spot welding, Metall. Mater. Trans. A 37 (9) (2006) 2773–2786.
[38] A. Fehrenbacher, J.R. Schmale, M.R. Zinn, F.E. Pfefferkorn, Measurement of tool-workpiece interface temperature distribution in friction stir welding, J. Manuf. Sci. Eng. 136 (2) (2014) 021009-021009-8.
[39] S.K. Everton, M. Hirsch, P. Stravroulakis, R.K. Leach, A.T. Clare, Review of in-situ process monitoring and in-situ metrology for metal additive manufacturing, Mater. Des. 95 (2016) 431–445.
[40] D.A. Kriczky, J. Irwin, E.W. Reutzel, P. Michaleris, A.R. Nassar, J. Craig, 3D spatial reconstruction of thermal characteristics in directed energy deposition through optical thermal imaging, J. Mater. Process. Technol. 221 (2015) 172–186.
[41] P. Frigola, O. Harrysson, T.J. Horn, H. West, R. Aman, J.M. Rigsbee, D.A. Ramirez, L. Murr, F. Medina, R.B. Wicker, E. Rodriguez, Fabricating copper components with Electron beam melting, Advanced Materials and Processes 172 (2014) 20–24.
[42] N.T. Aboulkhair, M. Simonelli, L. Parry, I. Ashcroft, C. Tuck, R. Hague, 3D printing of Aluminium alloys: Additive Manufacturing of Aluminium alloys using selective laser melting, Prog. Mater. Sci. 106 (2019) 100578.
[43] B. Verlinden, J. Driver, I. Samajdar, R.D. Doherty, Thermo-Mechanical Processing of Metallic Materials, Pergamon Materials Series, Pergamon, 2007, pp. 233–332.
[44] R.B. Dinwiddie, M.M. Kirka, P.D. Lloyd, R.R. Dehoff, L.E. Lowe, G.S. Marlow, Calibrating IR Cameras for In-situ Temperature Measurement During the Electron Beam Melt Processing of Inconel 718 and Ti-Al6-V4, SPIE, 2016.
[45] S.D. Holland, R.S. Reusser, Material evaluation by infrared thermography, Annu. Rev. Mater. Res. 46 (1) (2016) 287–303.
[46] M. Song, R. Kovacevic, Thermal modeling of friction stir welding in a moving coordinate system and its validation, Int. J. Mach. Tools Manuf. 43 (6) (2003) 605–615.
[47] T.J. Miller, S.J. Zinkle, B.A. Chin, Strength and fatigue of dispersion-strengthened copper, J. Nucl. Mater. 179–181 (1991) 263–266.
[48] R.F. Muraca, J.S. Whittick, Materials Data Handbook: Aluminum Alloy 6061, (1972).
[49] S. Mironov, K. Inagaki, Y.S. Sato, H. Kokawa, Microstructural evolution of pure copper during friction-stir welding, Philos. Mag. 95 (4) (2015) 367–381.
[50] H.J. Aval, S. Serajzadeh, A.H. Kokabi, Theoretical and experimental investigation into friction stir welding of AA 5086, Int. J. Adv. Manuf. Technol. 52 (5) (2011) 531–544.
[51] L. Commin, M. Dumont, J.E. Masse, L. Barrallier, Friction stir welding of AZ31 magnesium alloy rolled sheets: influence of processing parameters, Acta Mater. 57 (2) (2009) 326–334.
[52] V. Manvatkar, A. De, L.E. Svensson, T. DebRoy, Cooling rates and peak temperatures during friction stir welding of a high-carbon steel, Scr. Mater. 94 (2015) 36–39.
[53] Y.S. Sato, H. Kokawa, M. Enomoto, S. Jogan, Microstructural evolution of 6063 aluminum during friction-stir welding, Metall. Mater. Trans. A 30 (9) (1999) 2429–2437.
[54] W.J. Arbegast, Modeling Friction Stir Joining As a Metal Working Process, TMS Annual Meeting, San Diego, CA, 2003, pp. 313–327.
[55] K. Imada, M. Takayanagi, Plastic deformation of high density polyethylene in solid state extrusion, International Journal of Polymeric Materials and Polymeric Biomaterials 2 (2) (1973) 89–104.
[56] R. Nandan, G.G. Roy, T.J. Lienert, T. Debroy, Three-dimensional heat and material flow during friction stir welding of mild steel, Acta Mater. 55 (3) (2007) 883–895.
[57] G. Chen, Q. Shi, Z. Feng, On the material behavior at Tool/Workpiece interface during friction stir welding: a CFD based numerical study, in: R.S. Mishra, M.W. Mahoney, Y. Sato, Y. Hovanski (Eds.), Friction Stir Welding and Processing VIII, Springer International Publishing, Cham, 2016, pp. 251–258.
[58] P.A. Colegrove, 3 Dimensional Flow and Thermal Modelling of the Friction Stir Welding Process, University of Adelaide, Department of Mechanical Engineering, 2001.
[59] H. Schmidt, J. Hattel, Modelling heat flow around tool probe in friction stir welding, Sci. Technol. Weld. Join. 10 (2) (2005) 176–186.
[60] F.C. Liu, T.W. Nelson, Grain structure evolution, grain boundary sliding and material flow resistance in friction welding of Alloy 718, Mater. Sci. Eng. A 710 (2018) 280–288.
[61] G. Chen, Z. Feng, Y. Zhu, Q. Shi, An alternative frictional boundary condition for computational fluid dynamics simulation of friction stir welding, J. of Materi Eng and Perform 25 (2016) 4016–4023.
[62] A. Simar, Y. Bréchet, B. de Meester, A. Denquin, C. Gallais, T. Pardoen, Integrated modeling of friction stir welding of 6xxx series Al alloys: process, microstructure and properties, Prog. Mater. Sci. 57 (1) (2012) 95–183.
[63] P. Rosakis, A.J. Rosakis, G. Ravichandran, J. Hodowany, A thermodynamic internal variable model for the partition of plastic work into heat and stored energy in metals, J. Mech. Phys. Solids 48 (3) (2000) 581–607.
[64] O. Lorrain, V. Favier, H. Zahrouni, D. Lawrjaniec, Understanding the material flow path of friction stir welding process using unthreaded tools, J. Mater. Process. Technol. 210 (4) (2010) 603–609.
[65] P.F. Mendez, K.E. Tello, T.J. Lienert, Scaling of coupled heat transfer and plastic deformation around the pin in friction stir welding, Acta Mater. 58 (18) (2010) 6012–6026.
[66] J.R. Rumble, CRC Handbook of Chemistry and Physics, 100 ed., CRC Press/Taylor & Francis, Boca Raton, FL, 2019.
[67] D.M. Nuruzzaman, M.A. Chowdhury, Friction coefficient and wear rate of copper and aluminum sliding against mild steel international transaction, Journal of Engineering, Management, & Applied Sciences & Technologies 4 (1) (2012) 29–40.
[68] F. Cverna, ASM IMPD Committee, ASM Ready Reference: Thermal Properties of Metals, ASM International, (2002).